

Contents lists available at ScienceDirect

Petroleum Science

journal homepage: www.keaipublishing.com/en/journals/petroleum-science



Original Paper

Direct hydrocarbon identification in shale oil reservoirs using fluid dispersion attribute based on an extended frequency-dependent seismic inversion scheme



Zhi-Qi Guo a, *, Tao Zhang b, c, Cai Liu a

- ^a College of Geoexploration Science and Technology, Jilin University, Changchun, Jilin, 130021, China
- ^b SINOPEC Key Laboratory of Geophysics, Nanjing, Jiangsu, 211100, China
- ^c SINOPEC Geophysical Research Institute, Nanjing, Jiangsu, 211100, China

ARTICLE INFO

Article history: Received 29 May 2022 Received in revised form 10 September 2022 Accepted 26 December 2022 Available online 30 December 2022

Edited by Jie Hao

Keywords:
Shale oil
Fluid dispersion attribute
Hydrocarbon identification
Frequency-dependent inversion
Rock physics

ABSTRACT

The identification of hydrocarbons using seismic methods is critical in the prediction of shale oil reservoirs. However, delineating shales of high oil saturation is challenging owing to the similarity in the elastic properties of oil- and water-bearing shales. The complexity of the organic matter properties associated with kerogen and hydrocarbon further complicates the characterization of shale oil reservoirs using seismic methods. Nevertheless, the inelastic shale properties associated with oil saturation can enable the utilization of velocity dispersion for hydrocarbon identification in shales. In this study, a seismic inversion scheme based on the fluid dispersion attribute was proposed for the estimation of hydrocarbon enrichment. In the proposed approach, the conventional frequency-dependent inversion scheme was extended by incorporating the PP-wave reflection coefficient presented in terms of the effective fluid bulk modulus. A rock physics model for shale oil reservoirs was constructed to describe the relationship between hydrocarbon saturation and shale inelasticity. According to the modeling results, the hydrocarbon sensitivity of the frequency-dependent effective fluid bulk modulus is superior to the traditional compressional wave velocity dispersion of shales. Quantitative analysis of the inversion results based on synthetics also reveals that the proposed approach identifies the oil saturation and related hydrocarbon enrichment better than the above-mentioned conventional approach. Meanwhile, in real data applications, actual drilling results validate the superiority of the proposed fluid dispersion attribute as a useful hydrocarbon indicator in shale oil reservoirs.

© 2022 The Authors. Publishing services by Elsevier B.V. on behalf of KeAi Communications Co. Ltd. This is an open access article under the CC BY-NC-ND license (http://creativecommons.org/licenses/by-nc-nd/4.0/).

1. Introduction

Considering the increase in the development of shale oil reservoirs, the characterization of hydrocarbon enrichment using seismic methods is essential for identifying sweet spots in shale oil plays. However, because the elastic properties of oil- and waterbearing shales are similar, identifying shales of high oil saturation and hydrocarbon enrichment using seismically-inverted elastic attributes is challenging. Poroelastic behaviors associated with the complexity of organic matter further complicate the identification of oil-bearing shales using seismic methods. Therefore, the development of seismic methods for identifying hydrocarbons in shale

* Corresponding author.

E-mail address: guozhiqi@jlu.edu.cn (Z.-Q. Guo).

reservoirs is imperative.

Amplitude variation with offset (AVO) techniques involve diverse approximations of the Zoeppritz equation (Zoeppritz, 1919) and have been utilized in predicting hydrocarbon resources for many decades. Since Aki and Richards (1980) proposed a linearized expression based on velocities and density for the PP-wave reflection coefficient, many other approximations have been presented. Classical approximations were based on the following indicators: intercept and gradient (Shuey, 1985), P- and S-wave velocities and the corresponding impedances (Smith and Gidlow, 1987; Fatti et al., 1994), and Lamé coefficients moduli (Gray, 1999). Following the proposal of the Gassmann fluid term as a hydrocarbon indicator (Batzle et al., 2001), seismic AVO methods have been used for fluid identification (Russell et al., 2003, 2011; Zong et al., 2013; Yin and Zhang, 2014; Zhang et al., 2017).

The advancement in rock physics modeling methods has significantly enhanced the understanding of the mechanisms of seismic dispersion and attenuation related to fluid flow (Chapman et al., 2005, 2006; Jakobsen and Chapman, 2009; Ba et al., 2016, 2017). Considering that velocity dispersion produces the frequency dependence of reflection coefficients in inelastic media. Wilson et al. (2009) developed a frequency-dependent AVO (FD-AVO) scheme for characterizing fluids in hydrocarbon reservoirs based on seismic dispersion attributes. FD-AVO methods were primarily utilized in the detection of conventional (Zhang et al., 2011; Sun et al., 2012; Cheng et al., 2012; Wu et al., 2014; Chen et al., 2015; Luo et al., 2018) and unconventional (Pang et al., 2018; Liu et al., 2019; Jin et al., 2021) gas reservoirs. In gas detection applications, wave-induced fluid flow was considered the primary velocity dispersion and attenuation mechanism. In principle, different AVO approximations can be transformed to frequency-dependent forms that are suitable for FD-AVO inversions. Wang et al. (2019) compared the sensitivity of different dispersion attributes for the detection of fluids. In several studies, the FD-AVO has been optimized using spectral decomposition methods, such as variational mode decomposition (Liu et al., 2018), smoothed pseudo Wigner-Ville distribution (Liu et al., 2019), and inverse spectral decomposition (Luo et al., 2018; Huang et al., 2020).

In the characterization of oil reservoirs, oil has been detected using fluid factors derived from elastic properties (Huang et al., 2015: Pan and Zhang, 2019: Pan et al., 2019: Shu et al., 2021). However, the elastic properties of oil and water are similar: thus. the discrimination of oil- and water-bearing reservoirs remains challenging. According to rock physics modeling and laboratory studies, oil viscosity was found to be associated with noticeable velocity dispersion and attenuation of oil-bearing rocks (Chen et al., 2016; Yang et al., 2020). However, real data applications suggest that the P-wave frequency-dependent attributes may exhibit lower sensitivity to an oil zone than to a gas zone, which increases the challenge in the detection of oil saturation using the conventional dispersion attributes (Zhang et al., 2011; Sun et al., 2014). Therefore, it is necessary to develop new seismic dispersion attributes more sensitive to oil saturation for improved identification of favorable zones in shale oil reservoirs.

To adequately interpret the obtained dispersion attributes, rock physics modeling for organic shale is necessary to better understand the velocity dispersion and attenuation mechanisms in shale oil reservoirs. Carcione (2000) utilized an approach that incorporates viscoelasticity theory to describe the influence of oil generation on the inelastic properties of shales. This approach was based on early shale rock physics modeling studies by Vernik and Nur (1992) and Vernik and Liu (1997). Further, Carcione (2001) applied the model for AVO analysis of oil-bearing source rocks. The significance of the organic matter in the accumulation of hydrocarbons in shales has been further investigated using petrophysical analysis (Yenugu, 2014) and seismic rock physics modeling (Zhao et al., 2016; Zhang et al., 2018).

In the present study, a new seismic frequency-dependent inversion method is developed to improve hydrocarbon detection in shale oil reservoirs by estimating the fluid dispersion attribute. First, we present the scheme for the proposed fluid dispersion attribute inversion in detail. We then establish a rock physics model for analyzing the velocity dispersion and attenuation associated with the oil saturation and hydrocarbon enrichment in shale reservoirs. Subsequently, the proposed method was validated using synthetics computed by integrating the rock physics model with an advanced seismic modeling tool. The sensitivity of the proposed fluid dispersion attribute to oil saturation and hydrocarbon

enrichment is then analyzed and compared to that of the traditional compressional wave velocity dispersion. Finally, the applicability of the proposed method is demonstrated using field data from the intersalt shale oil reservoirs in the Jianghan Basin.

2. Theory and methodology

2.1. Seismic AVO representation for the estimation of pore-filling properties

We started from the formula of the PP-wave reflection coefficient that is associated with the Gassmann fluid term given by Russell et al. (2011), which has the expression as follows:

$$R_{pp}(\theta) = \left[\left(1 - \frac{\gamma_{\text{dry}}^2}{\gamma_{\text{sat}}^2} \right) \frac{\sec^2 \theta}{4} \right] \frac{\Delta f}{f} + \left(\frac{\gamma_{\text{dry}}^2}{4\gamma_{\text{sat}}^2} \sec^2 \theta - \frac{2}{\gamma_{\text{sat}}^2} \sin^2 \theta \right) \frac{\Delta \mu}{\mu} + \left(\frac{1}{2} - \frac{\sec^2 \theta}{4} \right) \frac{\Delta \rho}{\rho},$$

$$(1)$$

where θ is the average of the incidence and transmission angles across a reflector. $f=V_P^2\rho-\gamma_{\rm dry}^2V_S^2\rho$ denotes the averaged Gassmann fluid term. μ and ρ represent the averaged shear modulus and density across the boundary. Here, Δf and $\Delta \mu$ represent the differences in the corresponding properties across the interface. $\gamma_{\rm dry}=V_{P_{\rm dry}}/V_{S_{\rm dry}}$ indicates the velocity ratio of the dry frame, and $\gamma_{\rm sat}=V_{P_{\rm sat}}/V_{S_{\rm sat}}$ is the velocity ratio of the fluid-saturated medium.

Han and Batzle (2004) decoupled the Gassmann fluid term (f) using the gain function ($G(\varphi)$) related to porosity (φ) and the effective bulk modulus (K_f) of pore fluids; it is expressed as follows:

$$f = G(\varphi)K_f, \tag{2}$$

where $G(\varphi) = \left[1 - \left(\frac{K_{\text{dry}}}{K_0}\right)\right]^2 \varphi$, K_{dry} represents the bulk modulus of the dry frame, and K_0 denotes the bulk modulus of the mineral grains.

According to Zhang et al. (2017), Eq. (2) was substituted into Eq. (1) to produce the following expression:

$$R_{pp}(\theta) = \left[\left(1 - \frac{\gamma_{\text{dry}}^2}{\gamma_{\text{sat}}^2} \right) \frac{\sec^2 \theta}{4} \right] \frac{\Delta \left(G(\varphi) K_f \right)}{G(\varphi) K_f} + \left(\frac{\gamma_{\text{dry}}^2}{4 \gamma_{\text{sat}}^2} \sec^2 \theta - \frac{2}{\gamma_{\text{sat}}^2} \sin^2 \theta \right) \frac{\Delta \mu}{\mu} + \left(\frac{1}{2} - \frac{\sec^2 \theta}{4} \right) \frac{\Delta \rho}{\rho}.$$
(3)

Considering $\Delta(XY)/XY = \Delta X/X + \Delta Y/Y$ in Yilmaz (2008), Eq. (3) can be expressed as:

$$R_{pp}(\theta) = \left[\left(1 - \frac{\gamma_{\text{dry}}^2}{\gamma_{\text{sat}}^2} \right) \frac{\sec^2 \theta}{4} \right] \left(\frac{\Delta G(\varphi)}{G(\varphi)} + \frac{\Delta K_f}{K_f} \right) + \left(\frac{\gamma_{\text{dry}}^2}{4\gamma_{\text{sat}}^2} \sec^2 \theta - \frac{2}{\gamma_{\text{sat}}^2} \sin^2 \theta \right) \frac{\Delta \mu}{\mu} + \left(\frac{1}{2} - \frac{\sec^2 \theta}{4} \right) \frac{\Delta \rho}{\rho}.$$
(4)

Subsequently, Eq. (4) was rearranged to generate the following equation:

$$R_{pp}(\theta) = \left[\left(1 - \frac{\gamma_{\text{dry}}^2}{\gamma_{\text{sat}}^2} \right) \frac{\sec^2 \theta}{4} \right] \frac{\Delta K_f}{K_f} + \left[\left(1 - \frac{\gamma_{\text{dry}}^2}{\gamma_{\text{sat}}^2} \right) \frac{\sec^2 \theta}{4} \right] \frac{\Delta G(\varphi)}{G(\varphi)} \qquad R_{PP}(\theta, \omega) = R_{PP}(\theta, \omega_0) + (\omega - \omega_0) A(\theta) \frac{d}{d\omega} \left(\frac{\Delta K_f}{K_f} \right) + \left(\frac{\gamma_{\text{dry}}^2}{4\gamma_{\text{sat}}^2} \sec^2 \theta - \frac{2}{\gamma_{\text{sat}}^2} \sin^2 \theta \right) \frac{\Delta \mu}{\mu} + \left(\frac{1}{2} - \frac{\sec^2 \theta}{4} \right) \frac{\Delta \rho}{\rho}.$$

$$(5) \qquad \text{Eq. (10) can also be expressed as follows:}$$

Finally, Eq. (5) was simplified via linearization to the following expression:

$$R_{pp}(\theta) = A(\theta) \frac{\Delta K_f}{K_f} + A(\theta) \frac{\Delta G(\varphi)}{G(\varphi)} + B(\theta) \frac{\Delta \mu}{\mu} + C(\theta) \frac{\Delta \rho}{\rho}, \tag{6}$$

where
$$A(\theta) = \left(1 - \frac{\gamma_{\text{dry}}^2}{\gamma_{\text{sat}}^2}\right) \frac{\sec^2 \theta}{4}$$
, $B(\theta) = \frac{\gamma_{\text{dry}}^2}{4\gamma_{\text{sat}}^2} \sec^2 \theta - \frac{2}{\gamma_{\text{sat}}^2} \sin^2 \theta$ and $C(\theta) = \frac{1}{2} - \frac{\sec^2 \theta}{4}$.

In Eq. (6), K_f and $G(\varphi)$ are associated with the same coefficient $A(\theta)$, making these terms coupled in the elastic inversion. However, according to the expression given by Han and Batzle (2004), $G(\varphi)$ in Eq. (2) is irrelevant to fluids and can be considered independent of the frequency. Therefore, $G(\varphi)$ was dropped in the frequencydependent inversion scheme in section 2.2.

2.2. Frequency-dependent inversion scheme for pore-filling dispersion attribute

Considering that velocity dispersion and attention account for the frequency dependence of the PP-wave reflection coefficient (Wilson et al., 2009), Eq. (6) was extended to the frequency domain in the dispersion attribute inversion. In Eq. (6), it is reasonable to assume that K_f and μ are frequency-dependent, while $G(\varphi)$ and ρ are frequency-independent. Consequently, the frequency-dependent PP-wave reflection coefficient can be represented as follows:

$$R_{pp}(\theta,\omega) = A(\theta) \frac{\Delta K_f}{K_f}(\omega) + B(\theta) \frac{\Delta \mu}{\mu}(\omega) + A(\theta) \frac{\Delta G(\varphi)}{G(\varphi)} + C(\theta) \frac{\Delta \rho}{\rho}.$$
(7)

Eq. (7) was then expanded at a reference frequency (ω_0) using the first-order Taylor approximation, and the obtained reflection coefficient in the frequency domain is expressed as follows:

$$R_{pp}(\theta,\omega) = A(\theta) \frac{\Delta K_f}{K_f} (\omega_0) + (\omega - \omega_0) A(\theta) \frac{\mathrm{d}}{\mathrm{d}\omega} \left(\frac{\Delta K_f}{K_f} \right)$$

$$+ B(\theta) \frac{\Delta \mu}{\mu} (\omega_0) + (\omega - \omega_0) B(\theta) \frac{\mathrm{d}}{\mathrm{d}\omega} \left(\frac{\Delta \mu}{\mu} \right)$$

$$+ A(\theta) \frac{\Delta G(\varphi)}{G(\varphi)} + C(\theta) \frac{\Delta \rho}{\rho}.$$
(8)

The terms based on ω_0 and those irrelevant to frequency were grouped as shown in the following equation:

$$R_{pp}(\theta,\omega_{0}) = A(\theta) \frac{\Delta K_{f}}{K_{f}}(\omega_{0}) + B(\theta) \frac{\Delta \mu}{\mu}(\omega_{0}) + A(\theta) \frac{\Delta G(\varphi)}{G(\varphi)} + C(\theta) \frac{\Delta \rho}{\rho},$$
(9)

and Eq. (8) was then rearranged to produce the following expression:

$$R_{PP}(\theta,\omega) = R_{PP}(\theta,\omega_0) + (\omega - \omega_0)A(\theta)\frac{d}{d\omega}\left(\frac{\Delta K_f}{K_f}\right) + (\omega - \omega_0)B(\theta)\frac{d}{d\omega}\left(\frac{\Delta \mu}{\mu}\right).$$
(10)

Eq. (10) can also be expressed as follows:

$$\begin{split} \Delta R(\theta,\omega) &= R_{PP}(\theta,\omega) - R_{PP}(\theta,\omega_0) \\ &= (\omega - \omega_0) A(\theta) \frac{\mathrm{d}}{\mathrm{d}\omega} \left(\frac{\Delta K_f}{K_f} \right) + (\omega - \omega_0) B(\theta) \frac{\mathrm{d}}{\mathrm{d}\omega} \left(\frac{\Delta \mu}{\mu} \right). \end{split} \tag{11}$$

For the application with seismic data, an incidence wavelet with a spectrum $W(\omega)$ was introduced, and Eq. (11) was transformed into the time-frequency domain (S) using spectra decomposition to produce the following equation:

$$\Delta S(\theta, \omega) = S(\theta, \omega) - S(\theta, \omega_0)$$

$$= (\omega - \omega_0) W(\omega) \left\{ A(\theta) \frac{\mathrm{d}}{\mathrm{d}\omega} \left(\frac{\Delta K_f}{K_f} \right) + B(\theta) \frac{\mathrm{d}}{\mathrm{d}\omega} \left(\frac{\Delta \mu}{\mu} \right) \right\}. \tag{12}$$

Subsequently, dispersion attributes D_{Kf} and D_{μ} , which represent dispersions of the effective bulk modulus of pore fluids and shear modulus of the entire medium, respectively, were defined and expressed as follows:

$$D_{Kf} = \frac{\mathrm{d}}{\mathrm{d}\omega} \left(\frac{\Delta K_f}{K_f} \right),\tag{13}$$

$$D_{\mu} = \frac{\mathrm{d}}{\mathrm{d}\omega} \left(\frac{\Delta\mu}{\mu} \right),\tag{14}$$

Eq. (12) was then expressed using a matrix in the form of a prestack seismic gather with n incidence angles and m frequencies after spectral decomposition; it is expressed as follows:

$$\begin{bmatrix} \Delta S(\theta_{1}, \omega_{1}) \\ \vdots \\ \Delta S(\theta_{1}, \omega_{m}) \\ \vdots \\ \Delta S(\theta_{1}, \omega_{m}) \\ \vdots \\ \Delta S(\theta_{n}, \omega_{1}) \\ \vdots \\ \Delta S(\theta_{n}, \omega_{n}) \end{bmatrix} = \begin{bmatrix} (\omega_{1} - \omega_{0})W(\omega_{1})A(\theta_{1}) & (\omega_{1} - \omega_{0})W(\omega_{1})B(\theta_{1}) \\ \vdots & \vdots \\ (\omega_{m} - \omega_{0})W(\omega_{m})A(\theta_{1}) & (\omega_{m} - \omega_{0})W(\omega_{m})B(\theta_{1}) \\ \vdots & \vdots \\ (\omega_{1} - \omega_{0})W(\omega_{1})A(\theta_{n}) & (\omega_{1} - \omega_{0})W(\omega_{1})B(\theta_{n}) \\ \vdots & \vdots \\ (\omega_{m} - \omega_{0})W(\omega_{m})A(\theta_{n}) & (\omega_{m} - \omega_{0})W(\omega_{m})B(\theta_{n}) \end{bmatrix} \\ \times \begin{bmatrix} D_{Kf} \\ D_{\mu} \end{bmatrix}, \tag{15}$$

where *W* represents the spectrum of the wavelet.

Eq. (15) can be simplified into the following expression:

$$\mathbf{d} = \mathbf{G} \begin{bmatrix} D_{Kf} \\ D_{u} \end{bmatrix}. \tag{16}$$

The attributes D_{Kf} and D_{μ} in Eq. (16) can be computed using the least-squares method based on the following expression:

$$\begin{bmatrix} D_{Kf} \\ D_{u} \end{bmatrix} = \left(\mathbf{G}^{T} \mathbf{G} + \varepsilon^{2} \mathbf{I} \right)^{-1} \mathbf{G}^{T} \mathbf{d}, \tag{17}$$

where **I** represents the identity matrix and ε is the damping factor.

2.3. Spectral decomposition method

The success of implementing the dispersion attribute inversion approach depends on reasonably estimating the time-frequency spectra of seismic reflections. The Wigner-Ville distribution (WVD) is a practical approach for the decomposition of non-stationary seismic signals using an energy distribution function. For a time-domain seismic signal x(t), its WVD transform can be represented according to Cohen (1995) as follows:

$$WVD(t,f) = \int_{-\infty}^{\infty} X\left(t + \frac{\pi}{2}\right) \overline{X}\left(t - \frac{\pi}{2}\right) e^{-j2\pi f\tau} d\tau, \tag{18}$$

where X(t) is the analytic signal of the actual signal x(t) and τ denotes the time delay.

Cohen (1995) proposed a smooth pseudo-Wigner-Vile distribution (SPWVD) method to mitigate the impact of the cross term in the WVD that is associated with secondary nonlinear characteristics. This was achieved using a smoothing function in the time and frequency domains simultaneously, which is expressed as follows:

$$SW_{g,h,X} = \int_{-\infty}^{+\infty} \int_{-\infty}^{+\infty} X\left(t + \frac{\pi}{2}\right) \overline{X}\left(t - \frac{\pi}{2}\right) g(v)h(\tau)e^{-j2\pi f\tau} dv d\tau, \qquad (19)$$

where g(v) and $h(\tau)$ are time and frequency smoothing window functions, respectively; τ is the frequency shift; and v is the time delay. The Gauss function in the smoothing functions of g(v) and $h(\tau)$ has the following form:

$$\varphi(\nu,\tau) = e^{-\alpha\nu^2 - \beta\tau^2} (\alpha \ge 0, \ \beta \ge 0), \tag{20}$$

where α and β are the adjustment factors in the Gauss windows.

3. Geological setting

In the Qianjiang Sag of the Jianghan Basin, shale oil reservoirs in the intersalt formations have yielded abundant hydrocarbon content for many years. The area exhibits significant potential for additional oil production. According to the distribution of fault and structural zonings shown in Fig. 1a, the Qianjiang Sag involves five units in the region (Nie et al., 2020, 2021). The study area is located in the Banghu Syncline Zone, shown using the red rectangular in Fig. 1a.

Fig. 2 displays the stratigraphic units of the study area. The

		Stratig	Thickness	Sedimentary			
Era	System	Series	Formation	Member	m	facies	
Paleozoic	Oligocene	Lower	Qianjiang	Eq1	120–450		
	Eocene	Upper		Eq2	110–700		
				Eq3	150–640	Saline lake	
				Eq4 ^{upper}	100–700		
				Eq4 ^{lower}	173–2218		

Fig. 2. Stratigraphic units and sedimentary facies of the target formation in the study area.

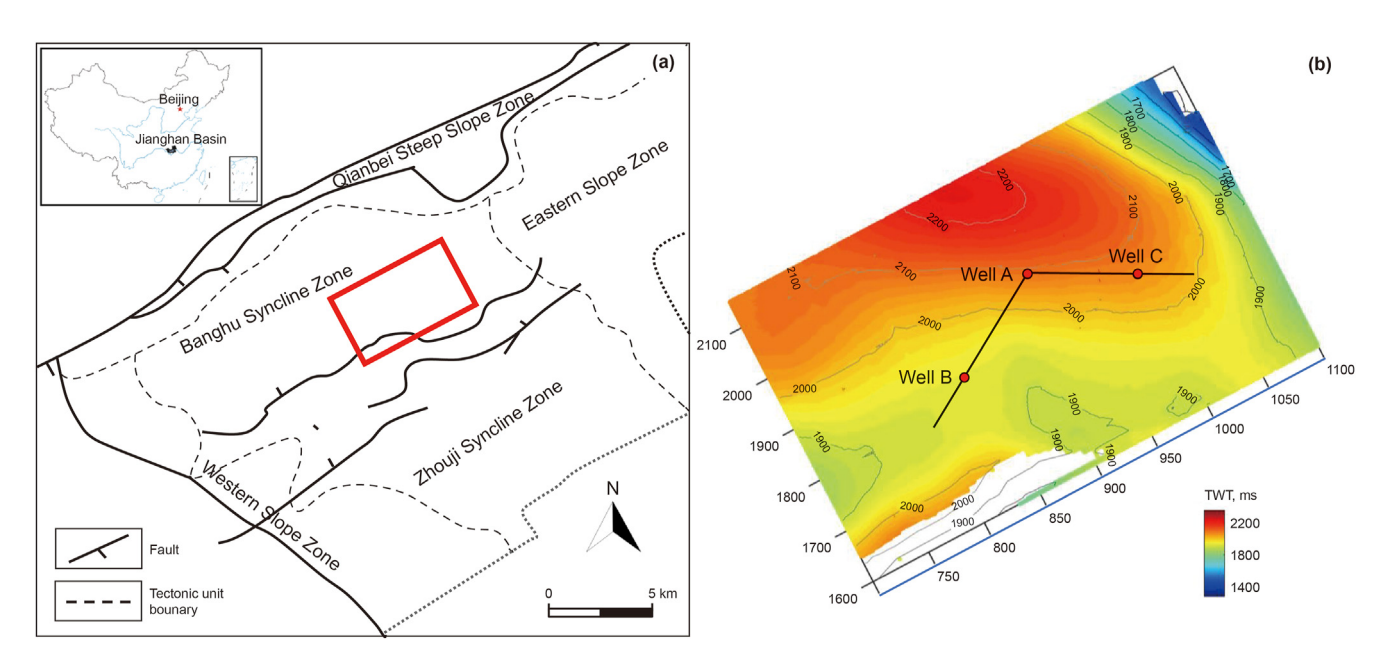


Fig. 1. (a) Regional geologic map of the Qianjiang Sag, Jianghan Basin and (b) map of the two-way travel time of seismic reflections from the top of the target shale oil reservoir. Locations of wells A, B, and C as well as cross-well seismic lines are also displayed on the map.

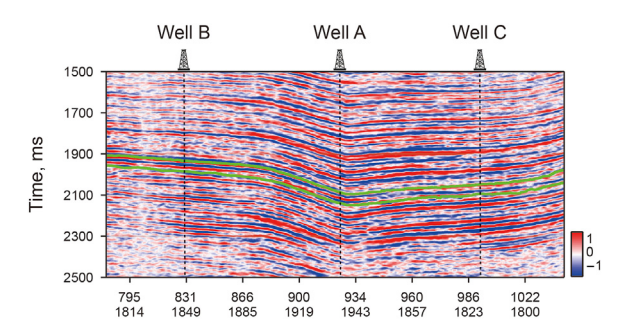


Fig. 3. Seismic section across wells A, B, and C. Two green lines denote the upper and lower boundaries of the target shale oil reservoir.

Qianjiang formation contains four members (Eq¹, Eq², Eq³, and Eq⁴). In this formation, generated hydrocarbons were preserved in the shale layers and sealed by salt layers, forming multilayer intersalt shale oil reservoirs. The two-way travel time of seismic reflections from the top of the Eq³, which is the target intersalt shale oil reservoir in the present study, is shown in Fig. 1b. Three wells (A, B, and C) were deployed and drilled in the study area, and the post-stack seismic profile across these wells is displayed in Fig. 3.

As shown in Fig. 3, interbedded structures of the salt and shale layers account for periodic seismic reflections. Two green lines represent the upper and lower boundaries of the target intersalt shale oil reservoir. Considerable oil has been produced from wells A and B, whereas well C yielded no oil. However, identifying oil pay zones based on the interpretation of amplitude is difficult because seismic signatures of the target shale formation at the locations of the three wells exhibited similar features. Therefore, the development of effective seismic methods for enhanced detection of hydrocarbons in the intersalt shale oil reservoir is critical. At the same time, logging data obtained from well A are displayed in Fig. 4, revealing the interbedded structure of the target formation.

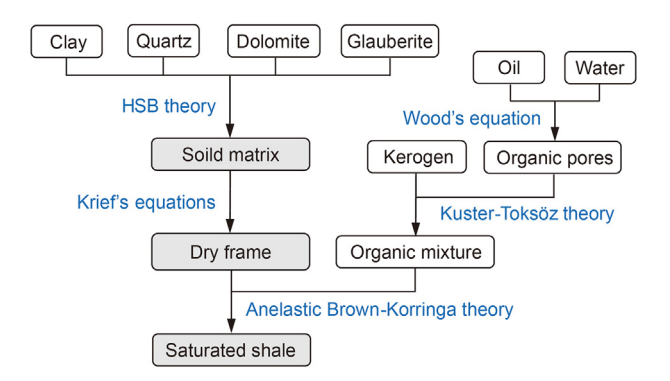


Fig. 5. Workflow of the rock physics modeling for shale oil reservoirs.

4. Theoretical model and analysis

4.1. Rock physics modeling method for shale oil reservoirs

The workflow of rock physics modeling for shale oil reservoirs is shown in Fig. 5. First, the Hashin-Shtrikman bounds (Hashin and Shtrikman, 1963) were used to estimate the elastic properties of a matrix comprising minerals. Intrinsic anisotropy of shale associated with clay minerals was not considered. Subsequently, the Krief equations (Krief et al., 1990) were utilized to obtain the dry frame moduli.

Petrophysical analysis indicates that the organic mixture of shales comprises kerogen and kerogen-related porosity generated during the maturation stage (Yenugu, 2014). According to Carcione (2001), the method proposed by Kuster and Toksoz (1974) was extended to compute the viscoelastic properties of the organic matter composed of kerogen and fluids. Therefore, in the present study, we used the method of Carcione (2001) to describe the velocity dispersion and attenuation associated with kerogen and oil.

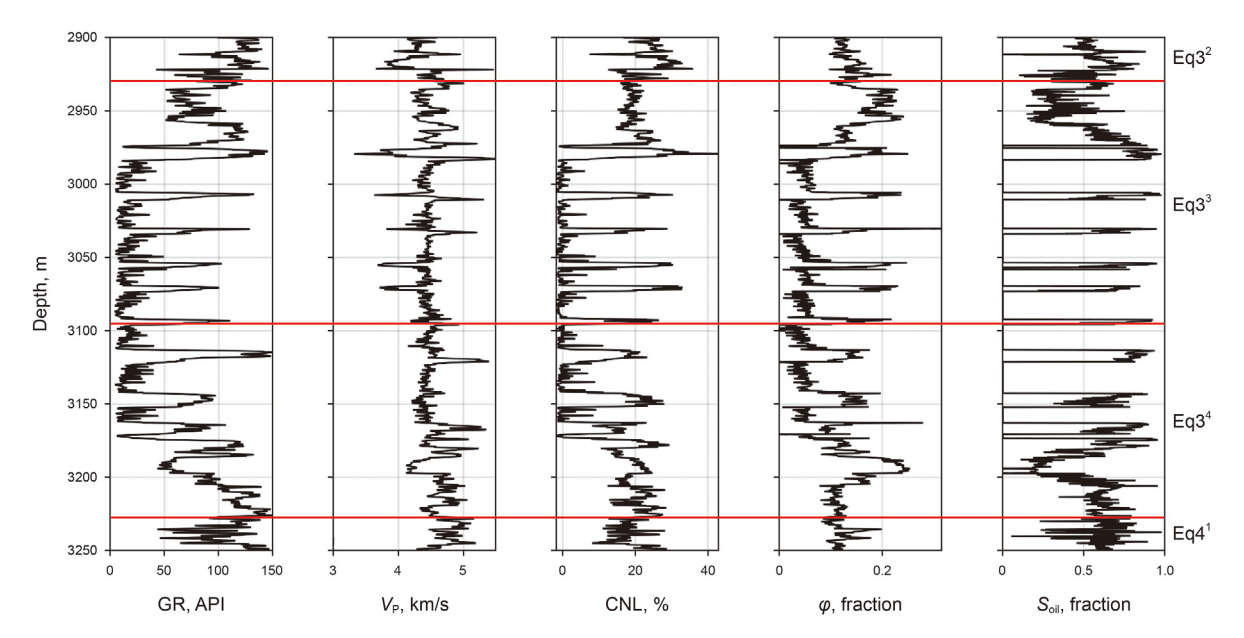


Fig. 4. Logging data of the target formation obtained from well A, including (a) gamma-ray (GR), (b) P-wave velocity (V_P), (c) compensated neutron log (CNL), (d) porosity (φ), and (e) oil saturation (S_{oil}). The subunits of the formations are labeled by superscripts.

Table 1Properties of components used in the rock physics modeling (Carcione, 2001; Mavko et al., 2009).

	Clay	Quartz	Dolomite	Glauberite	Kerogen	Oil	Water
$V_P(km/s)$	4.16	6.05	7.34	4.6	2.6	0.9	1.47
V_S (km/s)	2.32	4.09	3.94	2.05	1.2	_	_
ρ (g/cm ³)	2.58	2.65	2.87	2.35	1.4	0.7	1.04
Q_1	_	_	_	_	30	5	10
Q_2	_	_	_	_	20	_	_

The inelastic properties of shale were assumed to be primarily controlled by the compliance of kerogen and oil. Meanwhile, an extension of Wood's equation (Wood, 1941) was employed to compute the inelastic properties of the effective fluids composed of water and oil.

Finally, the organic mixture, consisting of kerogen and fluids, was assumed as inclusions exhibiting random orientations, neglecting the possible anisotropy attributed to the layering associated with the organic matter. The extended unelastic Brown-Korringa theory was utilized to obtain complex frequency-dependent stiffness values for organic-rich shales (Ciz and Shapiro, 2007), regarding the organic mixture as inclusions saturated in the dry frame. Properties used in the modeling are presented in Table 1. The viscoelastic theory used for quantifying the inelasticity of media is given in. Appendix A.

Fig. 5 illustrates the rock physics modeling framework for shale oil reservoirs. However, appropriate rock physics modeling should further consider the specific properties of reservoirs in the local areas. Fig. 6 reveals a positive correlation between the oil saturation ($S_{\rm oil}$) and the kerogen content (KC) obtained from well log data of the shale oil reservoirs in the study area. The fitted linear relationship between the two factors is obtained and presented as:

$$KC = 0.08S_{oil} + 0.01 \tag{21}$$

In rock physics modeling, we considered the collaborative change of $S_{\rm oil}$ and KC (Fig. 6). The increase in $S_{\rm oil}$ corresponds to the increase in KC simultaneously. In specific operations, $S_{\rm oil}$ was set to 0.5 as the reference model as denoted by the red dot in Fig. 6. In this case, KC equals 0.05 according to Eq. (21). The porosity was set to 0.15. The volumetric fractions of clay, quartz, dolomite, and glauberite were set to 0.26, 0.24, 0.24, and 0.06, respectively, according to the properties obtained from logging interpretation.

Based on the reference model, the modeling considered the correlation between $S_{\rm oil}$ and KC for different $S_{\rm oil}$ models, according

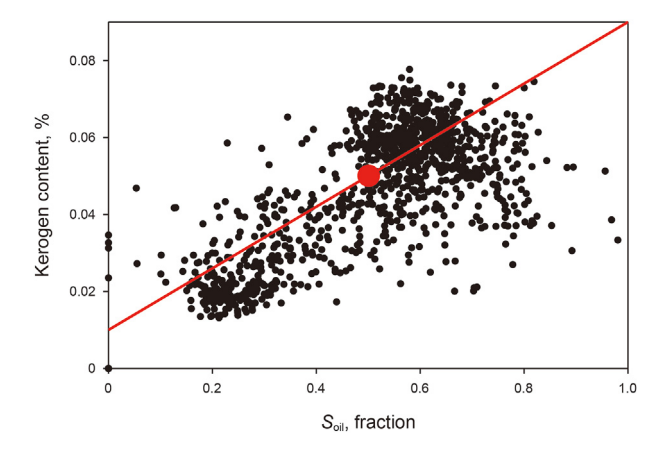


Fig. 6. Cross plot of oil saturation (S_{oil}) and kerogen content (KC) using logging data from the shale oil reservoirs. The red line represents the fitted linear relationship. The red dot denotes the values used in the reference model.

to the fitted relationship in Fig. 6. Specifically, as $S_{\rm oil}$ increases from 0 to 1, KC rises from 0.01 to 0.09 according to Eq. (21). Correspondingly, the sum proportion of minerals decreases as KC increases. Meanwhile, the relative volumetric proportions of minerals were set to be the same as those in the above reference model. In all the models with different $S_{\rm oil}$ values, the porosity was kept constant to be 0.15, and the pore space was saturated with water and oil.

4.2. Modeling analysis of different dispersion attributes

For the $S_{\rm oil}$ models in section 4.1, the dispersion and attenuation corresponding to the P-wave velocity of the entire shale (Fig. 7) and effective bulk modulus of fluids (Fig. 8) were computed using the proposed model illustrated in Fig. 5. As shown in Fig. 7a, the P-wave velocity (V_P) of the shale decreases as $S_{\rm oil}$ increases at all involved frequencies. The magnitude of the dispersion in Fig. 7a and the corresponding P-wave attenuation factor (Q_P^{-1}) in Fig. 7b also increase as the $S_{\rm oil}$ increases. In comparison, the effective bulk modulus of fluids (K_f) and the corresponding attenuation factor (Q_K^{-1}) for different $S_{\rm oil}$ values were displayed in Fig. 8a and b. Predictably, changes in the magnitudes of K_f and Q_K^{-1} as the $S_{\rm oil}$ increases are higher than those of V_P and Q_P^{-1} . These results demonstrate that a direct inversion of fluid-related properties produces a superior indicator of oil saturation and hydrocarbon enrichment in shale reservoirs.

In Figs. 7b and 8b, $Q_{\overline{P}}^{-1}$ and $Q_{\overline{K}_{j}}^{-1}$ were calculated using the following expressions:

$$Q_P^{-1}(\omega) = \frac{\operatorname{Im}\left[V_P(\omega)^2\right]}{\operatorname{Re}\left[V_P(\omega)^2\right]},\tag{22}$$

$$Q_{Kf}^{-1}(\omega) = \frac{\operatorname{Im}\left[K_f(\omega)^2\right]}{\operatorname{Re}\left[K_f(\omega)^2\right]}.$$
 (23)

The relaxation time τ_0 , as shown in Eq. (A-5) in Appendix A, determines the characteristic frequency f_0 by the relationship $f_0 = 1/\tau_0$. The f_0 value represents the frequency associated with maximum dispersion and attenuation (Carcione, 1997). According to poroelastic theories on the mechanism of seismic attenuation, f_0 is inversely proportional to the fluid viscosity η (Carcione et al., 2010), as shown in the following expression:

$$f_0 \approx \kappa K_f / (\varphi \eta d^2),$$
 (24)

where K_f is the effective fluid bulk modulus, κ represents permeability, φ denotes porosity, and d is the size of the patches for heterogeneous distribution of fluids.

According to Teja and Rice (1981), the value of η for the mixture of oil and water can be calculated using the following equation:

$$\eta = \eta_{o} \left(\frac{\eta_{w}}{\eta_{o}} \right)^{S_{oil}}, \tag{25}$$

where η_0 and η_W are viscosities of the oil and water, respectively.

The value of f_0 in Eq. (24) can be significantly affected by η because η_0 is usually several orders of magnitude higher than η_W (Carcione and Picotti, 2006). According to Eqs. (24) and (25), f_0 decreases as S_{0il} increases, thereby shifting the frequency range of the maximum dispersion and the corresponding attenuation peaks to a lower frequency (Figs. 7 and 8).

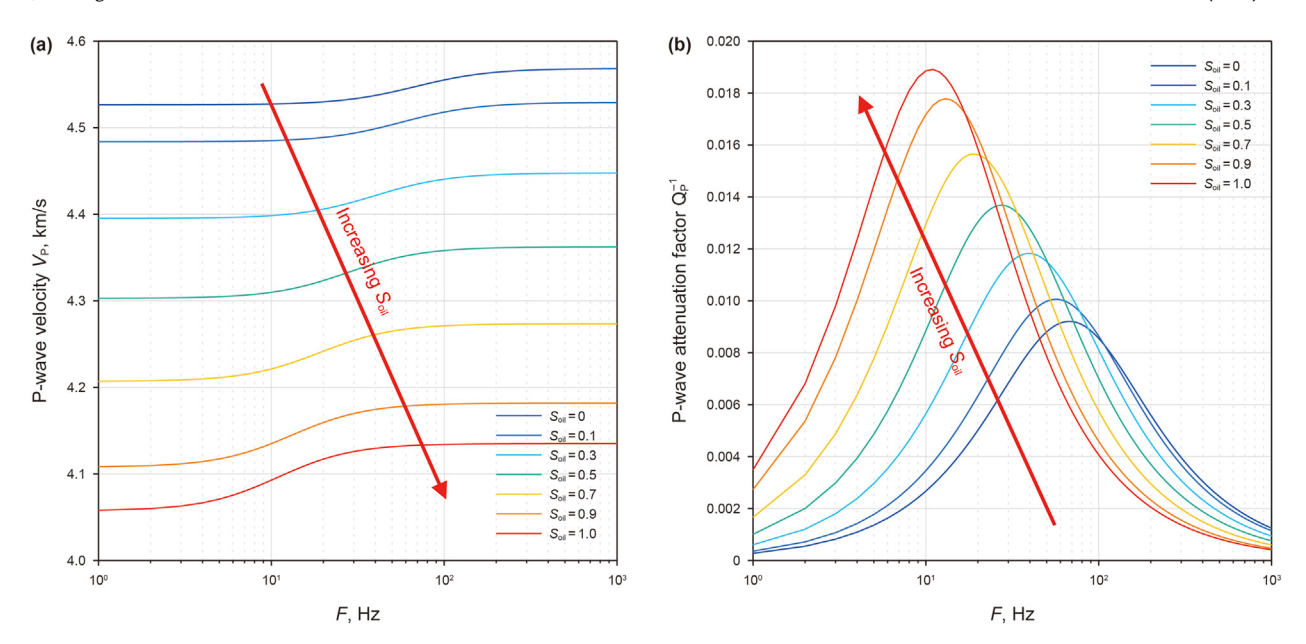


Fig. 7. Plots of the (a) V_P and (b) corresponding Q_P^{-1} versus frequency for different S_{oil} values.

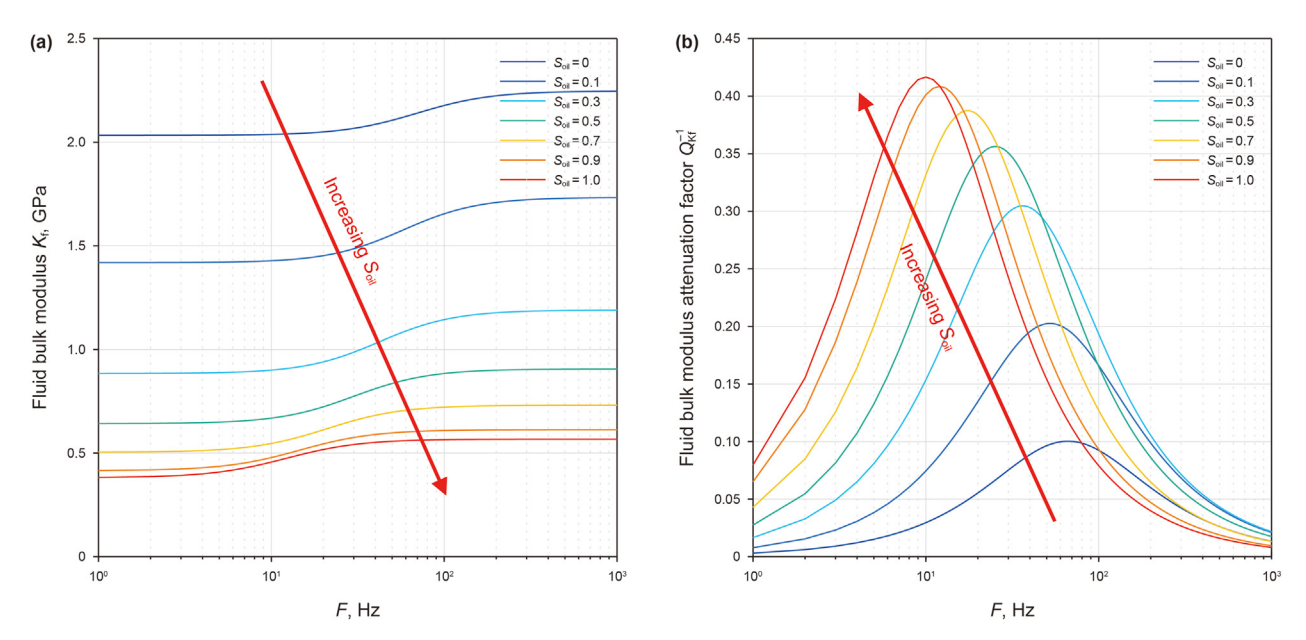


Fig. 8. Plots of the (a) K_f and (b) corresponding Q_{Kf}^1 versus frequency for different S_{oil} values.

4.3. Synthetic model test

As displayed in Fig. 9, a model of the intersalt shale oil reservoir for synthetic seismic modeling was designed according to the typical structures of the target formation in the study area. The model exhibits a rhythmic layering of salt and shale units, and each thin unit was assigned a thickness of 10 m. The salt layer was assumed to be purely elastic with a P-wave velocity of 5000 m/s, an S-wave velocity of 2700 m/s, and a density of 2200 kg/m³, according to the statistical results of the elastic properties. Properties of the shale layer were computed using the model proposed in the present study, with frequency-dependent P-wave velocity displayed in Fig. 7a for different $S_{\rm oil}$ models.

For an interface separating salt and shale, we computed the terms $\Delta V_P/V_P$ and $\Delta K_f/K_f$ versus frequency for different S_{oil} models,

as shown in Fig. 10a and b. K_f of shale was computed with Wood's equation (Wood, 1941) for different $S_{\rm oil}$ values. The salt layer was assumed water-saturated with the corresponding K_f equal to that of water. Results in Fig. 10 indicate that $\Delta K_f/K_f$ exhibits an order of magnitude higher than $\Delta V_P/V_P$ in terms of the frequency-dependent variation for different $S_{\rm oil}$ models. $\Delta K_f/K_f$ equals zero when $S_{\rm oil}=0$ because both layers are saturated with water in this case. Therefore, an improved sensitivity is expected from the fluid dispersion attribute D_{Kf} represented by the difference of $\Delta K_f/K_f$ to frequency, as shown in Eq. (13).

The synthetics and inversion results are displayed in Fig. 11. In Fig. 11a, the values of P-impedance (I_P) for $S_{\rm oil}$ values of 0, 0.5, and 1 were computed using the P-wave velocity at 40 Hz (Fig. 7a). Density and shear wave velocity were computed but not displayed for simplicity. As mentioned, the collaborative change of $S_{\rm oil}$ and KC

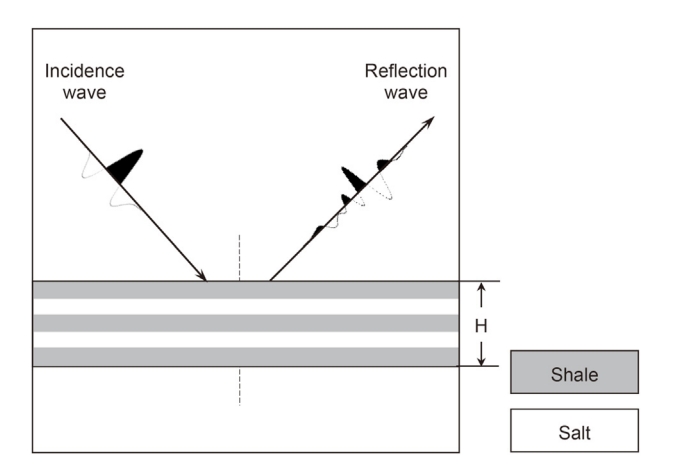


Fig. 9. Model of the intersalt shale oil reservoir, which exhibits a rhythmic layering of salt and shale.

was considered in different $S_{\rm oil}$ models. Seismic modeling was conducted based on the propagator matrix method (PMM) and the rock physics model for shale. The utilized PMM was developed based on Carcione (2001), with applications presented in Guo et al. (2015, 2018). Pre-stack gathers with incidence angles ranging from 0° to 30° were calculated for a 40 Hz Ricker wavelet. The corresponding stacked traces are shown in Fig. 11b. We can observe the differences in the reflection amplitudes for the three $S_{\rm oil}$ models.

The spectral decomposition results corresponding to the three S_{oil} models are shown in Fig. 11c—e. The decomposed spectra were computed using the SPWVD method described in section 2.3. Fig. 11f illustrates the D_P results obtained from the method of Wilson et al. (2009), while Fig. 11g shows the D_{Kf} values computed using the method described in section 2.2. As shown in the results, a higher anomaly was observed for the dispersion attributes D_P and D_{Kf} at higher S_{oil} values. Nevertheless, the limited bandwidth of the incidence wavelet presents challenges in discriminating the anomalies from an individual shale unit. Interestingly, D_P and D_{Kf} exhibit different response characteristics for varied S_{oil} , as shown in Fig. 11f and g. For instance, the D_P value changes more evidently for

 $S_{\rm oil}$ varying from a moderate to high value (0.5–1.0) compared to that observed for $S_{\rm oil}$ from a low to moderate value (0–0.5), as shown in Fig. 11f. This implies that the ability of D_P to discriminate $S_{\rm oil}$ from low to moderate values may be limited.

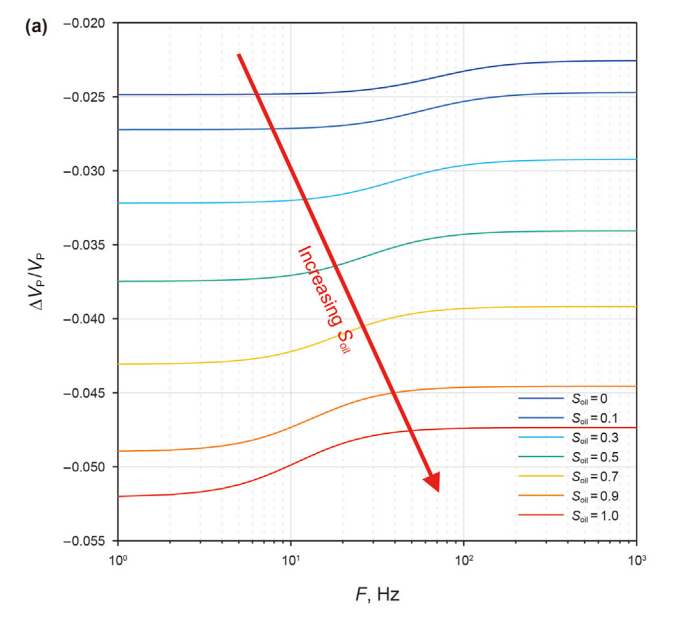
In contrast, D_{Kf} represents comparable sensitivity for $S_{\rm oil}$ varying from low to moderate (0–0.5) and moderate to high values (0.5–1.0), as shown in Fig. 11g. This suggests that D_{Kf} has the potential as a robust indicator of oil saturation and hydrocarbon enrichment in the shale oil reservoirs.

Furthermore, we quantitatively analyzed the different responses of D_P and D_{Kf} to continuous variations in $S_{\rm oil}$ values, as shown in Fig. 12a and b, respectively. The dispersion attributes were calculated as the root-mean-square values within the time covering the target intersalt shale oil reservoirs in Fig. 11a. As shown in Fig. 12, D_P and D_{Kf} values were normalized to the range between 0 and 1 to facilitate quantitative comparisons.

As shown in Fig. 13, the histogram indicates that the $S_{\rm oil}$ values obtained from the well log data for the target shale layer in the study area tend to concentrate within the range of 0.2 and 0.8, suggesting the common occurrence of moderate oil saturation in the oil pay zones. As shown in Fig. 12a and b, the quantitative analysis indicates that corresponding to the $S_{\rm oil}$ range of 0.2–0.8, relative changes in D_P and D_{Kf} are 52% and 71%, respectively. The higher variation in D_{Kf} further substantiates its enhanced sensitivity to variation in $S_{\rm oil}$ and hydrocarbon enrichment.

5. Field data applications

We then presented a field data application to the 3D pre-stack seismic data obtained from an intersalt shale oil reservoir in the study area shown in Fig. 1. Figs. 14-16 illustrate the logging data, cross-well stacked seismic traces, decomposed spectra, and inversion results at wells A, B, and C, respectively. Drilling results indicate that oil production is high in wells A and B, whereas well C does not produce oil. Accordingly, the inverted D_P and D_{Kf} values obtained from wells A and B show high-value anomalies, as shown in Figs. 14 and 15, respectively. Lower values were obtained from well C, as shown in Fig. 16. Therefore, the inversion results coincide with the results obtained from the drilling analysis. As shown in Figs. 14-16, although D_P and D_{Kf} exhibit similar characteristics, the



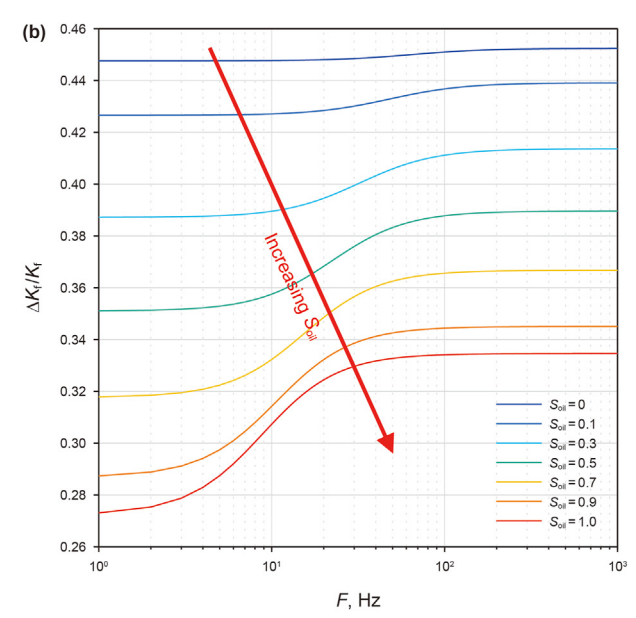


Fig. 10. Plots showing the (a) $\Delta V_P/V_P$ and (b) $\Delta K_f/K_f$ versus frequency for different S_{oil} values.

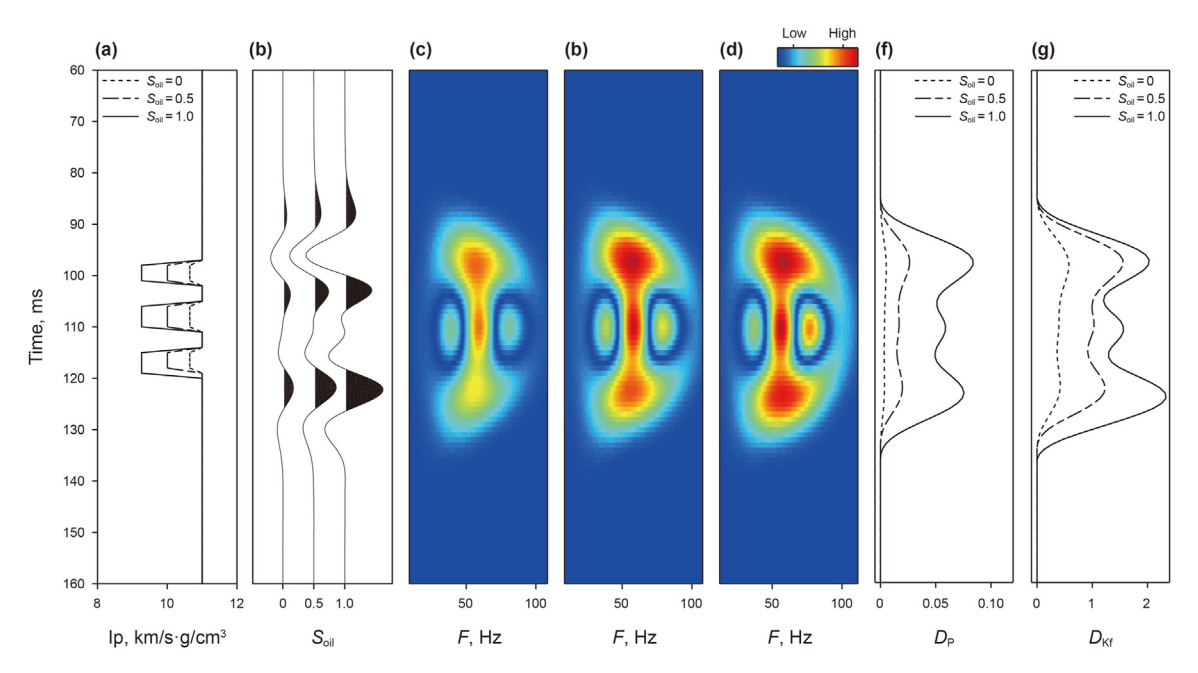


Fig. 11. (a) I_P for three S_{oil} models, (b) Corresponding stacked traces modeled by PMM. (c)—(e) Time-frequency spectra for the three S_{oil} models. (f) Inverted D_P and (g) D_{KJ} for the three S_{oil} models.

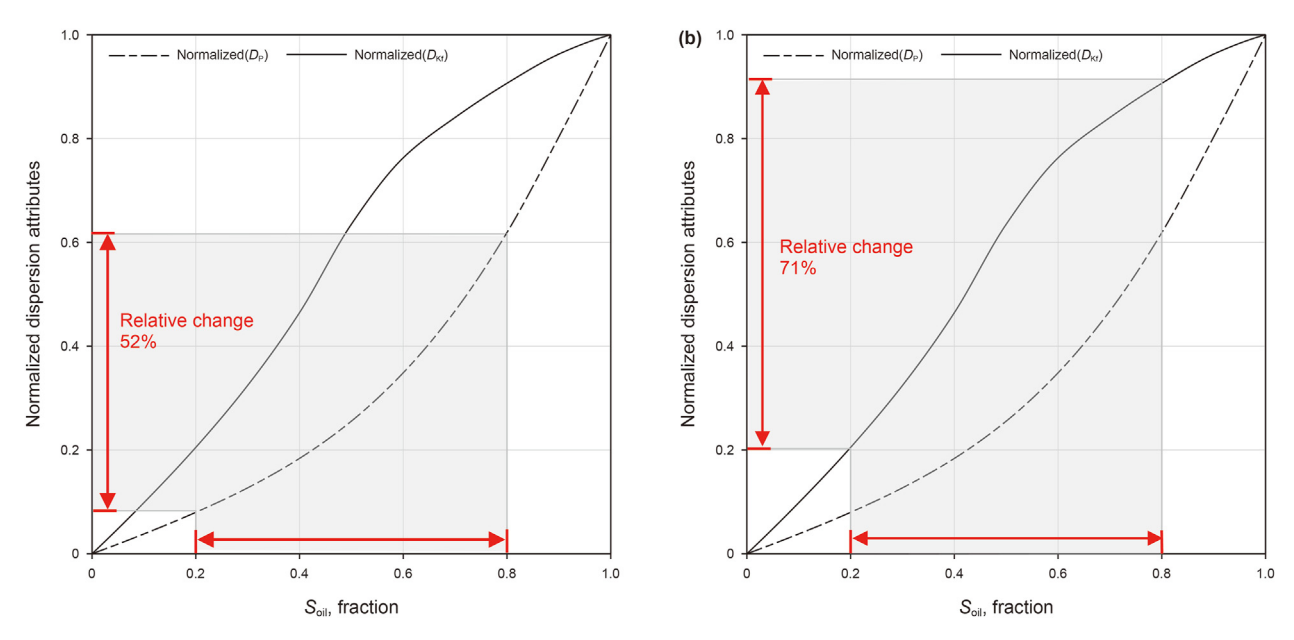


Fig. 12. Normalized D_P and D_{Kf} for increasing S_{oil} values. Relative changes of D_P and D_{Kf} are quantitatively compared for S_{oil} between 0.2 and 0.8.

magnitude of D_{Kf} is much significantly higher than that of D_R thereby indicating the higher sensitivity of D_{Kf} to oil pay zones. Meanwhile, the enhanced sensitivity of D_{Kf} to S_{oil} and hydrocarbon enrichment has also been validated using the synthetics of theoretical models (Fig. 11).

Then, the performance of D_P and $D_{K\!f}$ in estimating the lateral variation of hydrocarbon enrichment was further compared on seismic sections. As illustrated in Fig. 17, the decomposed spectra of the seismic section (Fig. 3) may be used to identify hydrocarbons in the shale oil reservoir. The decomposed spectra at certain specific frequencies may exhibit similar trends as the dispersion attributes. However, the physical implications of the decomposed spectra may not be explicitly delineated, thus challenging the applicability of

hydrocarbon identification using these spectra straightforwardly.

The sections of inverted D_P and D_{Kf} are demonstrated in Figs. 18 and 19, where the values were normalized to the range between 0 and 1 for comparison. As indicated by black arrows, the oil pay zones interpreted from the drilling results in wells A and B showed high-value anomalies in D_P and D_{Kf} . Notably, no responses in D_P and D_{Kf} were generated in the target layer in non-productive well C. In comparison, the seismic amplitudes in the post-stack section (Fig. 3) exhibit insufficient lateral variations to distinguish oil-producing pay zones in wells A and B from the non-reservoir zone in well C.

Although D_P and D_{Kf} values showed strong anomalies in the oilbearing pay zones, they exhibited distinct responses in the target

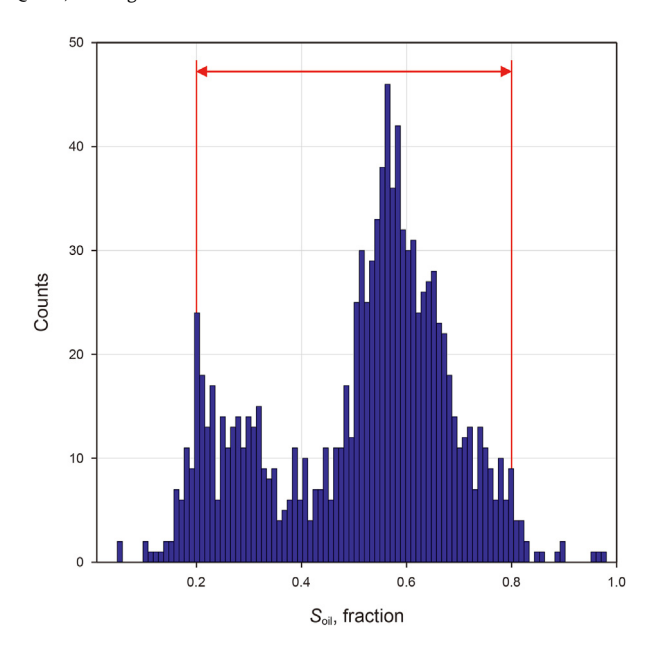


Fig. 13. Histogram of S_{oil} from logging data of the target shale reservoirs. The dominant value of S_{oil} ranges between 0.2 and 0.8.

shale oil reservoirs. The D_{Kf} value (Fig. 19) showed apparent anomalies with improved spatial continuity and temporal resolution in the pay zones compared to those obtained from D_P (Fig. 18). The sensitivity and robustness of D_{Kf} over D_P for the hydrocarbon identification observed in field data applications were consistent with the quantitative analysis using the synthetic data (Fig. 12).

In addition, we compared three dispersion attributes, as shown in Fig. 20. The corresponding values were normalized to the range between 0 and 1 for comparison. The average sum of normalized D_P and $D_{K\!f}$ showed a relatively linear correlation with $S_{\rm oil}$; thus, it may provide a quantitative estimate of $S_{\rm oil}$, depending on the availability of logging data for further calibration. In the corresponding section

shown in Fig. 21, the oil pay zones in wells A and B can be identified reliably, with the anomaly responses slightly different from D_{Kf} in Fig. 19.

A horizontal slice of the average sum of normalized D_P and $D_{K\!f}$ for the target intersalt shale oil reservoir is illustrated in Fig. 22. The attribute distribution indicates promising areas with high hydrocarbon enrichment, which are mainly located in the western part of the study area. The results provide essential information on hydrocarbon accumulation and thus help characterize potentially oilrich zones for future exploration and development of the intersalt shale oil reservoirs.

6. Discussion

We proposed a new seismic inversion scheme to compute the fluid dispersion attribute D_{Kf} for improved hydrocarbon identification in shale oil reservoirs. The proposed method extended the conventional FD-AVO inversion scheme by incorporating the PP-wave reflection coefficient represented by the effective fluid bulk modulus (K_f) in Zhang et al. (2011). Analyses using rock physics modeling and synthetics indicated that D_{Kf} exhibits increased sensitivity to oil saturation and hydrocarbon enrichment compared to the traditional compressional wave velocity dispersion D_P (Figs. 10 and 12). Field data applications confirmed that D_{Kf} can be used as a preferable hydrocarbon indicator for intersalt shale oil reservoirs in the study area (Fig. 19).

When extending Eqs. (6) and (7) for establishing the FD-AVO inversion scheme, the frequency-dependent reflection coefficient was assumed to be related to the elastic moduli varying with the frequency without considering the particular velocity dispersion and attenuation mechanisms. Therefore, in the hydrocarbon identification for specific reservoirs, it is necessary to conduct appropriate rock physics modeling to better interpret the computed dispersion attributes in local areas. In this study, the inelastic properties of the organic shale were attributed to the compliance of kerogen and oil (Carcione, 2000, 2001). However, the interactions between organic components, microcracks, and fractures in shale should be further considered using advanced rock physics models

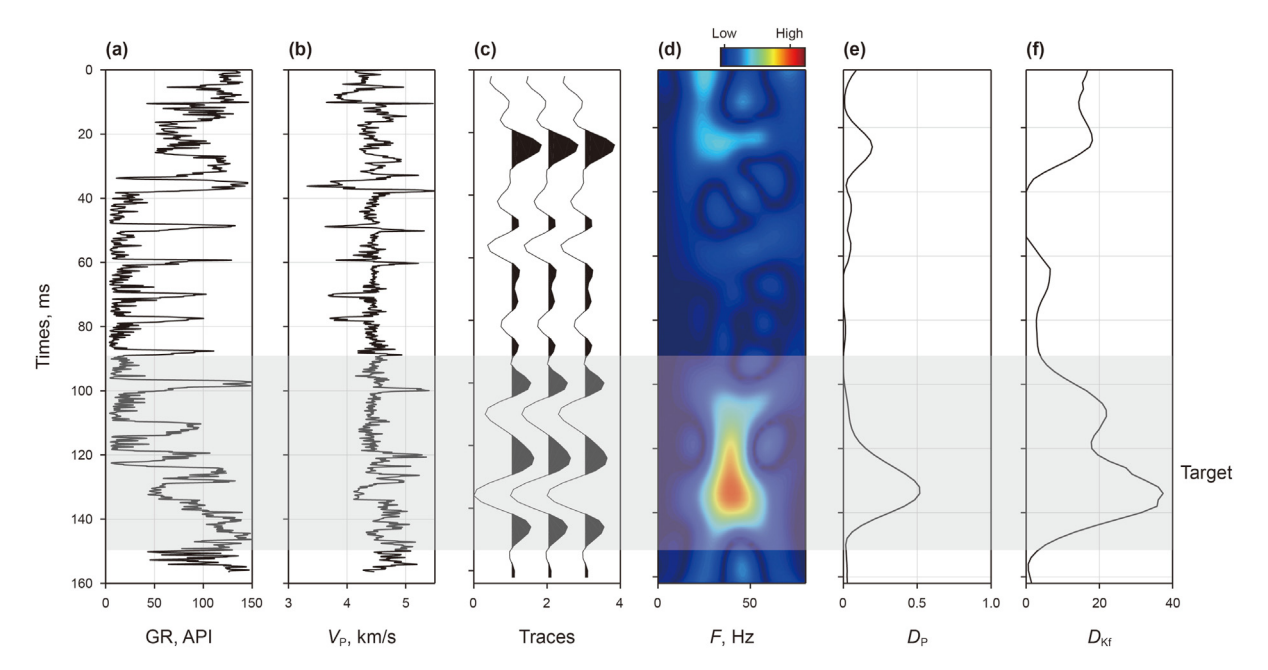


Fig. 14. Logging data of (a) GR and (b) V_P from Well A, (c) cross-well stacked seismic traces, (d) decomposed spectrum, (e) D_P and (f) D_{KF} . The target formation of the intersalt shale oil reservoir is shadowed in gray. Well A has been proven as an oil-producing well.

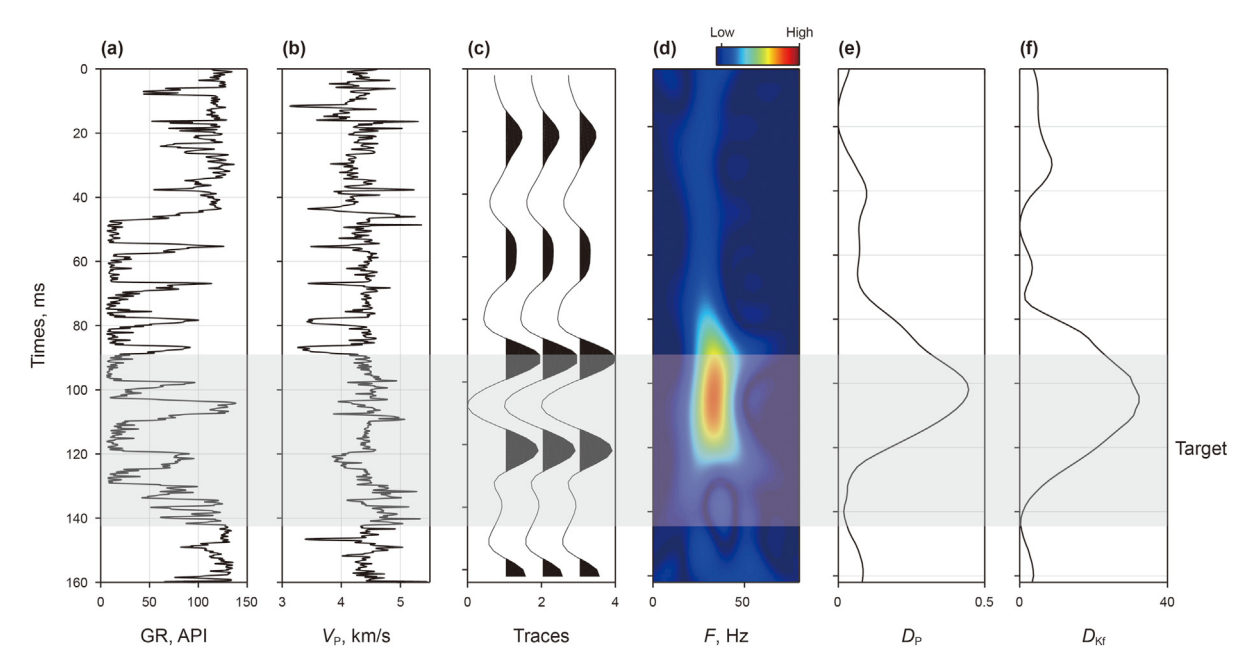


Fig. 15. Logging data of (a) GR and (b) V_P from Well B, (c) cross-well stacked seismic traces, (d) decomposed spectrum, (e) D_P and (f) D_{KP} . The target formation of the intersalt shale oil reservoir is shadowed in gray. Well B has been proven as an oil-producing well.

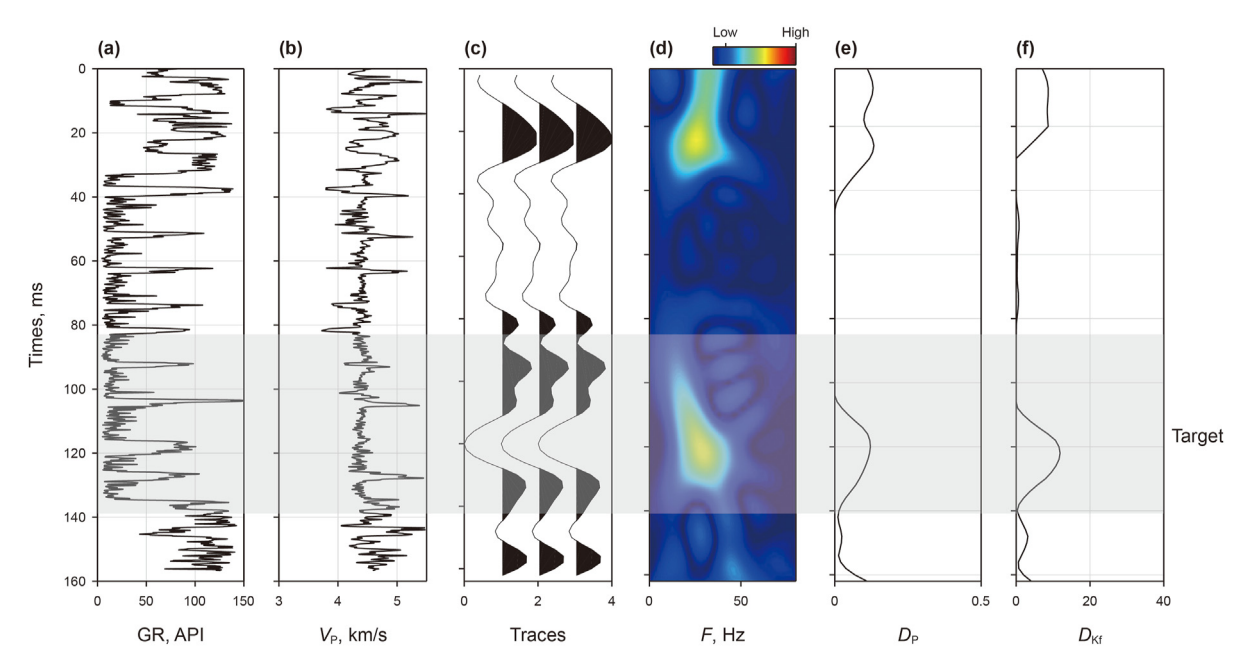


Fig. 16. Logging data of (a) GR and (b) V_P from Well C, (c) cross-well stacked seismic traces, (d) decomposed spectrum, (e) D_P and (f) D_{KJ} . The target formation of the intersalt shale oil reservoir is shadowed in gray. Well C has been proven as a non-productive well.

to better understand the significance of the obtained dispersion attributes. At the same time, the shear modulus dispersion in Eq. (14) was not discussed, owing to the insufficient understanding of the poroelastic behavior of shear waves propagating in organic shale. More laboratory measurements and sophisticated rock physics models will help provide insights into the velocity dispersion and attenuation related to shear waves for the comprehensive applications of P- and S-wave dispersion attributes.

Owing to the limited temporal resolution of seismic reflections for the interbedded thin layers, identifying an individual oilbearing shale layer was challenging, as demonstrated by the synthetic tests in Fig. 11 and real data applications in Figs. 14–16. Moreover, structure-related interferences can also cause frequency-dependent seismic reflections, which may lead to uncertainty in the interpretation of dispersion attributes. Spectral decomposition techniques with higher resolutions may be incorporated to mitigate such problems in future applications.

Meanwhile, as illustrated in Fig. 6, a positive correlation exists between kerogen content (KC) and oil saturation ($S_{\rm oil}$). Such correlation may produce coupled seismic responses of these two factors. In future studies, a feasible solution to this problem is to extend the AVO formula represented in terms of fluid factor (Russell

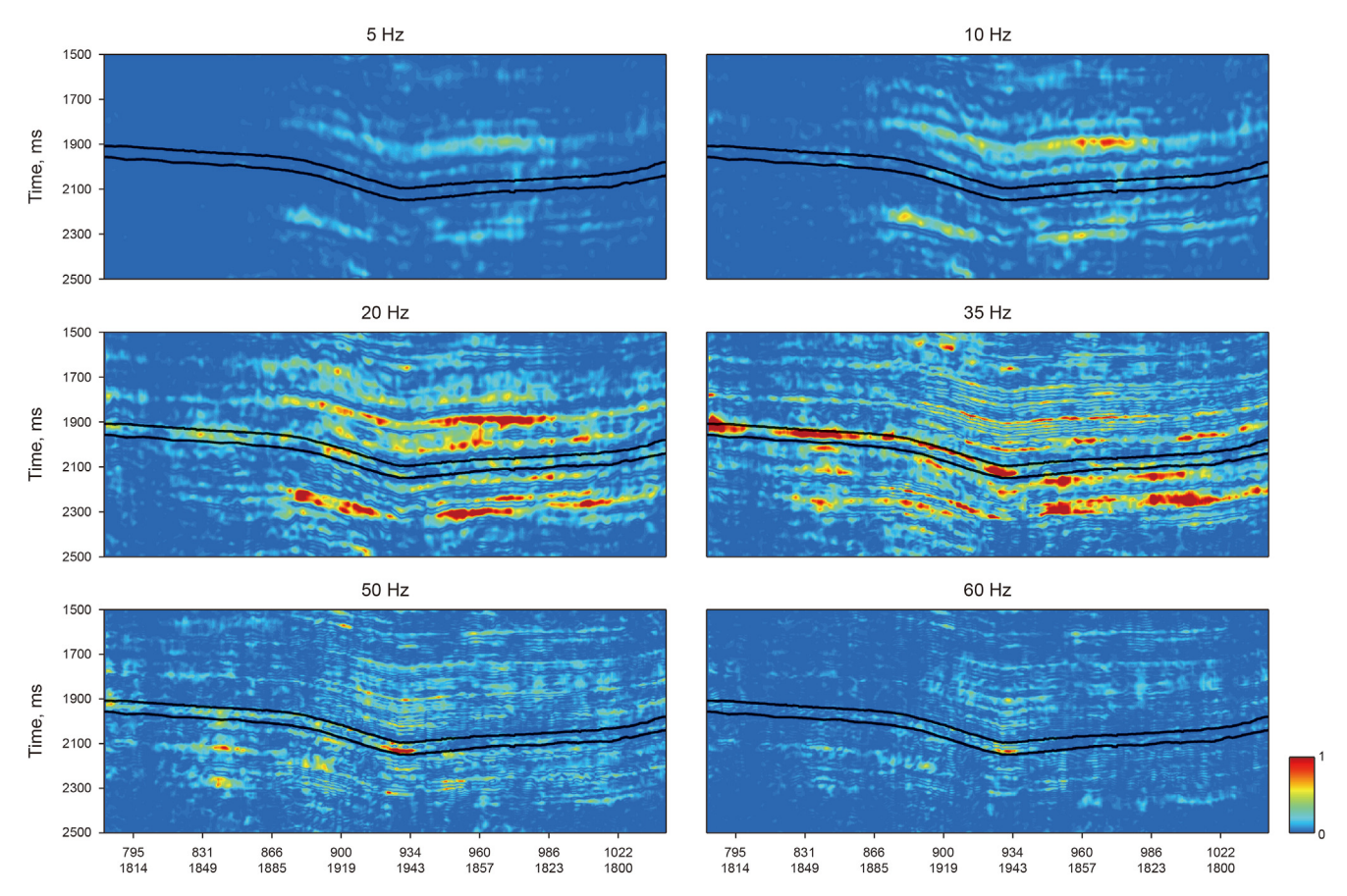


Fig. 17. Decomposed spectra of the seismic section in Fig. 3 at frequencies of (a) 5 Hz, (b) 10 Hz, (c) 20 Hz, (d) 35 Hz, (e) 50 Hz, and (f) 60 Hz.

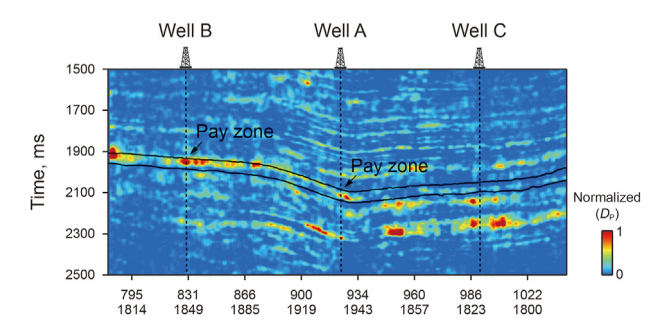


Fig. 18. The section of normalized D_P across wells A, B, and C. Two black lines denote the upper and lower boundaries of the target intersalt shale oil reservoir. Two arrows indicate the locations of oil-bearing pay zones in wells A and B.

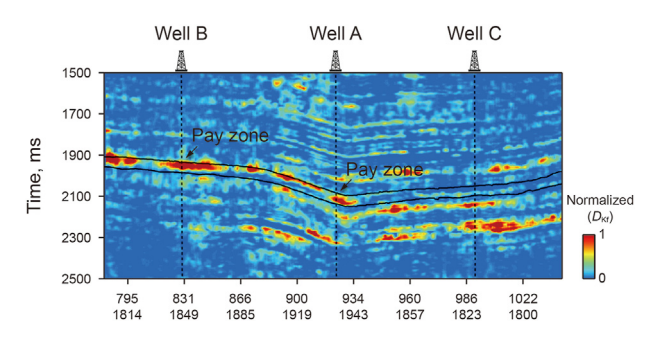


Fig. 19. The section of normalized D_{KJ} across wells A, B, and C. Two black lines denote the upper and lower boundaries of the target intersalt shale oil reservoir. Two arrows indicate the locations of oil-bearing pay zones in wells A and B.

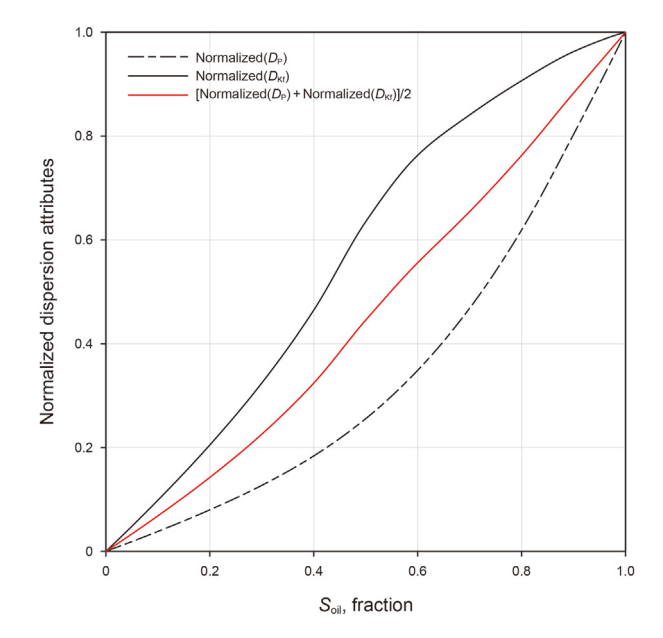


Fig. 20. Normalized dispersion attributes D_P , D_{KJ} , and the average sum of normalized D_P and D_{KJ} for increasing S_{oil} values.

et al., 2011) or effective fluid bulk modulus (Yin and Zhang, 2014; Zhang et al., 2017) with the solid substitution theory by considering the organic mixture composed of kerogen and fluids as solid pore-fillings. Based on this, new elastic and associated dispersion

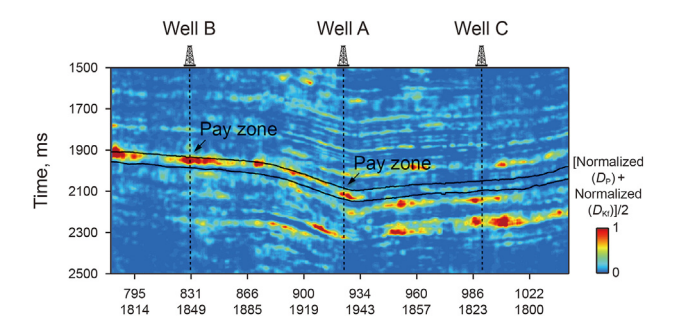


Fig. 21. The section of the average sum of normalized D_P and D_{Kf} across wells A, B, and C. Two black lines denote the upper and lower boundaries of the target intersalt shale oil reservoir. Two arrows indicate the locations of oil-bearing pay zones in wells A and D_P

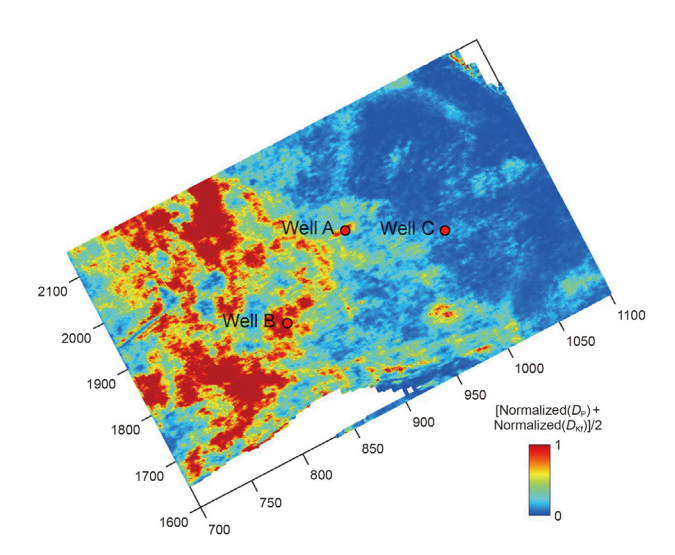


Fig. 22. Horizontal slice of the average sum of normalized D_P and D_{Kf} for the target intersalt shale oil reservoir in the study area.

attributes could be defined and estimated for improved hydrocarbon identification in organic-rich shales.

7. Conclusions

Prediction of hydrocarbon enrichment using seismic methods is significant for identifying favorable oil-bearing shales. A rock physics model was constructed to describe the inelastic properties associated with organic matter and oil saturation in shale oil reservoirs. Analyses based on the constructed model showed that the frequency dependence of the effective fluid bulk modulus exhibits an improved sensitivity to oil saturation and hydrocarbon enrichment compared to the compressional wave velocity dispersion of the entire shale. Accordingly, a new seismic inversion scheme was proposed by extending the conventional frequency-dependent inversion method to compute the fluid dispersion attribute D_{Kf} to predict oil saturation and hydrocarbon enrichment in shale reservoirs. Quantitative analysis using synthetics justified the superiority of D_{Kf} for hydrocarbon identification over the conventional compressional wave dispersion attribute D_P . For the intersalt shale oil model in the study area, the relative changes in D_P and D_{Kf} were estimated as 52% and 71%, respectively, for the oil saturation predominantly varying from 0.2 to 0.8. This result validated the improved sensitivity of D_{Kf} to oil saturation and hydrocarbon enrichment. The drilling results corroborated the results of the

proposed method for hydrocarbon identification in the intersalt shale oil reservoir in Qianjiang Sag, suggesting D_{Kf} as a preferable hydrocarbon indicator.

The proposed method can be applied for hydrocarbon identification in other oil and gas reservoirs based on appropriate rock physics modeling and analysis. The strategy of extending elastic AVO to dispersion attribute inversion presented in this study may inspire further development of other practical dispersion attributes.

Acknowledgments

This work was supported by the National Natural Science Foundation of China (Grant numbers 42074153 and 42274160) and the Open Research Fund of SINOPEC Key Laboratory of Geophysics (Grant number 33550006-20-ZC0699-0006).

APPENDIX A. Viscoelastic Theory

According to the standard linear solid model and Boltzmann theory (Carcione, 1997), the complex stiffness for a viscoelastic medium with transverse anisotropy is given by:

$$c_{I(I)} = \widehat{c}_{I(I)} - D + BM_1 + \frac{4}{3}GM_2, I = 1, 2, 3,$$
 (A-1)

$$c_{IJ} = \widehat{c}_{IJ} - D + BM_1 + 2G\left(1 - \frac{1}{3}M_2\right), I, J = 1, 2, 3; I \neq J$$
 (A-2)

$$c_{55} = \widehat{c}_{55} M_2, c_{66} = \widehat{c}_{66} M_2 \tag{A-3}$$

with

$$B = D - \frac{4}{3}G, D = \frac{1}{3}\left(2\widehat{c}_{11} + \widehat{c}_{33}\right), \text{ and } G = \frac{1}{3}\left(2\widehat{c}_{55} + \widehat{c}_{66}\right), \tag{A-4}$$

where \hat{c}_{IJ} are the elastic stiffnesses at the high-frequency limit. The complex Zener moduli in Eqs. (A-1) to (A-3) is:

$$M_{\nu}(\omega) = \frac{\sqrt{Q_{\nu}^{2} + 1} - 1 + i\omega Q_{\nu} \tau_{0}}{\sqrt{Q_{\nu}^{2} + 1} + 1 + i\omega Q_{\nu} \tau_{0}},$$
(A-5)

where the subscript v=1,2 represent the relaxation mechanism of P- and S-wave, respectively; ω is the angular frequency; τ_0 is the relaxation time.

In this study, we only consider the isotropic limitation of the viscoelastic anisotropic theory.

References

Aki, K., Richards, P.G., 1980. Quantitative Seismology. W.H. Freeman and Co.

Ba, J., Xu, W., Fu, L., et al., 2017. Rock anelasticity due to patchy saturation and fabric heterogeneity: a double double-porosity model of wave propagation. J. Geophys. Res. Solid Earth 122, 1949–1976. https://doi.org/10.1002/2016JB013882.

Ba, J., Zhao, J., Carcione, J.M., et al., 2016. Compressional wave dispersion due to rock matrix stiffening by clay squirt flow. Geophys. Res. Lett. 43 (12), 6186–6195. https://doi.org/10.1002/2016GL069312.

Batzle, M., Hofmann, R., Han, D.H., et al., 2001. Fluids and frequency dependent seismic velocity of rocks. Lead. Edge 20 (2), 168–171. https://doi.org/10.1190/ 1.1438900.

Carcione, J.M., 1997. Reflection and transmission of qPqS plane waves at a plane boundary between viscoelastic transversely isotropic media. Geophys. J. Int. 129, 669–680. https://doi.org/10.1111/j.1365-246X.1997.tb04502.x.

Carcione, J.M., 2000. A model for seismic velocity and attenuation in petroleum source rocks. Geophysics 65 (4), 1080–1092. https://doi.org/10.1190/1.1444801.

Carcione, J.M., 2001. AVO effects of a hydrocarbon source-rock layer. Geophysics 66 (2), 419-427. https://doi.org/10.1190/1.1444933.

- Carcione, J.M., Morency, C., Santos, J.E., 2010. Computational poroelasticity a review. Geophysics 75 (5), 75A229-75A243. https://doi.org/10.1190/1.3474602.
- Carcione, I.M., Picotti, S., 2006. P-wave seismic attenuation by slow-wave diffusion: effects of inhomogeneous rock properties. Geophysics 71 (3), https://doi.org/ 10.1190/1.2194512. 01-08.
- Chapman, M., Liu, E.R., Li, X.Y., 2005. The influence of abnormally high reservoir attenuation on the AVO signature. Lead. Edge 24 (11), 1120–1125. https:// doi.org/10.1190/1.2135103.
- Chapman, M., Liu, E.R., Li, X., 2006. The influence of fluid-sensitive dispersion and attenuation on AVO analysis. Geophys. J. Int. 167, 89-105. https://doi.org/ 10.1111/j.1365-246X,2006.02919.x.
- Chen, S., Chapman, M., Wu, X., et al., 2015. The application of quantitative gas saturation estimation based on the seismic wave dispersion inversion. J. Appl. Geophys. 120, 81–95. https://doi.org/10.1016/j.jappgeo.2015.07.001.
- Chen, X.H., Zhong, W.L., He, Z.H., et al., 2016. Frequency-dependent attenuation of compressional wave and seismic effects in porous reservoirs saturated with multi-phase fluids. J. Petrol. Sci. Eng. 147, 371-380. https://doi.org/10.1016/ i.petrol.2016.08.031.
- Cheng, B., Xu, T., Li, S., 2012. Research and application of frequency dependent AVO analysis for gas recognition (in Chinese). Chin. J. Geophys. 55 (2), 608-613. https://doi.org/10.6038/i.issn.0001-5733.2012.02.023.
- Ciz, R., Shapiro, S.A., 2007. Generalization of Gassmann equations for porous media saturated with a solid material. Geophysics 72 (6), A75–A79. https://doi.org/ 10 1190/1 2772400
- Cohen, L., 1995. Time-frequency Analysis. Prentice Hall Inc., New York, USA https:// doi.org/10.1007/1-4020-4513-1 99.
- Fatti, J.L., Smith, G.C., Vail, P.J., Strauss, P.J., Levitt, P.R., 1994. Detection of gas in sandstone reservoirs using AVO analysis: a 3-D seismic case history using the Geostack technique. Geophysics 59, 1362-1376. https://doi.org/10.1190/ 11443695
- Gray, D., 1999. Bridging the Gap: using AVO to detect changes in fundamental elastic constants, SEG 1999 Expanded Abstracts 852-855, https://doi.org/10.1190/ 1.1821163.
- Guo, Z.Q., Liu, C., Li, X.Y., et al., 2015. An improved method for the modeling of frequency-dependent amplitude-versus-offset variations. Geosci. Rem. Sens. Lett. IEEE 12, 63-67. https://doi.org/10.1109/LGRS.2014.2326157.
- Guo, Z.Q., Liu, X.W., 2018. Seismic rock physics characterization of anisotropic shale a Longmaxi Shale case study. J. Geophys. Eng. 15, 512-526. https://doi.org/ 10.1088/1742-2140/aa9fe1.
- Han, D., Batzle, M., 2004. Gassmann's equation and flfluid-saturation effects on seismic velocities. Geophysics 69 (2), 398-405. https://doi.org/10.1190/ 1.1707059
- Hashin, Z., Shtrikman, S., 1963. A variational approach to the theory of the elastic behavior of multiphase materials. J. Mech. Phys. Solid. 11, 127-140. https:// doi.org/10.1016/0022-5096(63)90060-7.
- Huang, G.T., Chen, X.H., Luo, C., et al., 2020. Mesoscopic wave-induced fluid flow effect extraction by using frequency-dependent prestack waveform inversion. IEEE Trans. Geosci. Rem. Sens. 59 (8), 6510-6524. https://doi.org/10.1109/ TGRS.2020.3028032
- Huang, X.R., Huang, J.P., Li, Z.C., 2015. High-sensitivity Fluid Identification Factor in Anisotropic Tight-Oil Sandstone Reservoirs. Seg Technical Program Expanded. https://doi.org/10.1190/segam2015-5909080.1.
- Jakobsen, M., Chapman, M., 2009. Unified theory of global flow and squirt flow in cracked porous media. Geophysics 74, WA65-WA76. https://doi.org/10.1190/
- Jin, H., Liu, C., Guo, Z.Q., et al., 2021. Rock physical modeling and seismic dispersion attribute inversion for the characterization of a tight gas sandstone reservoir. Front. Earth Sci. 9, 641651. https://doi.org/10.3389/feart.2021.641651.
- Krief, M., Garat, J., Stellingwerff, J., et al., 1990. A petrophysical interpretation using the velocities of P and S waves (full waveform sonic). Log. Anal. 31 (6),
- Kuster, G.T., Toksoz, M.N., 1974. Velocity and attenuation of seismic waves in twophase media-1,2. Geophysics 39 (5), 587-618. https://doi.org/10.1190/
- Liu, J., Ning, J., Liu, X., Liu, C., et al., 2019. An improved scheme of frequencydependent AVO inversion method and its application for tight gas reservoirs. Geofluids 2019 (2), 1-12. https://doi.org/10.1155/2019/3525818
- Liu, W., Cao, S., Jin, Z., et al., 2018. A novel hydrocarbon detection approach via highresolution frequency- dependent AVO inversion based on variational mode decomposition. IEEE Trans. Geosci. Rem. Sens. 56 (4), 2007-2024. https:// doi.org/10.1109/TGRS.2017.2772037.
- Luo, Y., Huang, H., Yang, Y., et al., 2018. Integrated prediction of deepwater gas reservoirs using Bayesian seismic inversion and fluid mobility attribute in the south China sea. J. Nat. Gas Sci. Eng. 59, 56-66. https://doi.org/10.1016/ j.jngse.2018.08.019.
- Mavko, G., Mukerji, T., Dovrkin, J., 2009. The Rock Physics Handbook: Tools for Seismic Analysis in Porous Media. Cambridge University Press, https://doi.org/ 10.1007/s00024-009-0456-7
- Nie, X., Lu, J., Chi, J.Y., et al., 2021. Oil content prediction method based on the TOC and porosity of organic-rich shales from wireline logs: a case study of lacustrine

- intersalt shale plays in Qianjiang Sag, Jianghan Basin, China. Geofluids ume 2021. https://doi.org/10.1155/2021/9989866. Article ID 9989866, 8 pages.
- Nie, X., Lu, J., Djaroun, R.R., et al., 2020. Oil content prediction of lacustrine organicrich shale from wireline logs: a case study of intersalt reservoirs in the Qianjiang Sag, Jianghan Basin, China. Interpretation 8 (3), SL79-SL88. https:// doi.org/10.1190/int-2019-0247.1.
- Pan, X., Zhang, G., 2019. Fracture detection and fluid identification based on anisotropic Gassmann equation and linear-slip model. Geophysics 84 (1), R99-R112. https://doi.org/10.1190/geo2018-0255.1.
 Pan, X., Zhang, G., Yin, X., 2019. Amplitude variation with offset and azimuth
- inversion for fluid indicator and fracture weaknesses in an oil-bearing fractured reservoir, Geophysics 84 (3), N41-N53. https://doi.org/10.1190/geo2018-0554.1.
- Pang, S., Liu, C., Guo, Z., et al., 2018. Gas identification of shale reservoirs based on frequency-dependent AVO inversion of seismic data. Chin. J. Geophys. 61 (11), 4613-4624. https://doi.org/10.6038/cjg2018L0529 (in Chinese)
- Russell, B.H., Gray, D., Hampson, D.P., 2011. Linearized AVO and poroelasticity. Geophysics 76, C19-C29. https://doi.org/10.1190/1.3555082.
- Russell, B.H., Hedlin, K., Hilterman, F.J., 2003. Fluid-property discrimination with AVO: a Biot-Gassmann perspective. Geophysics 68, 29-39. https://doi.org/ 10.1190/1.1543192.
- Shu, N.K., Su, C.G., Shi, X.G., et al., 2021. Seismic description and fluid identification of thin reservoirs in Shengli Chengdao extra-shallow sea oilfield. Petroleum explortion and development 48 (4), 889-899. https://doi.org/10.1016/S1876-3804(21)60074-5
- Shuey, R.T., 1985. A simplification of the Zoeppritz equations. Geophysics 50, 609-614, https://doi.org/10.1190/1.1441936
- Smith, G.C., Gidlow, P.M., 1987. Weighted stacking for rock property estimation and detection of gas. Geophys. Prospect. 35, 993-1014. https://doi.org/10.1111/ i.1365-2478.1987.tb00856.x.
- Sun, S.Z., Yue, H., Zhang, Y., et al., 2014. An Improved Frequency-dependent AVO Inversion Algorithm for Fluid Detection. Seg Technical Program Expanded. https://doi.org/10.1190/segam2014-1509.1.
- Sun, Z.D., Jiang, S., Sun, X., 2012. Fluid Identification Using Frequency-dependent AVO Inversion in Dissolution Caved Carbonate. Seg Technical Program Expanded, pp. 1-5. https://doi.org/10.1190/segam2012-1017.1.
- Teja, A.S., Rice, P., 1981. Generalized corresponding states method for the viscosities of liquid mixtures. Indian Engineering and Chemistry Fundamentals 20, 77-81. https://doi.org/10.1021/i100001a015.
- Vernik, L., Liu, X., 1997. Velocity anisotropy in shales: a petrophysical study. Geophysics 62, 521-532. https://doi.org/10.1190/1.1444162
- Vernik, L., Nur, A., 1992. Ultrasonic velocity and anisotropy of hydrocarbon source
- rocks. Geophysics 57 (5), 727–735. https://doi.org/10.1190/1.1443286. Wang, P., Li, J., Chen, X., et al., 2019. Fluid Discrimination Based on Frequencydependent AVO Inversion with the Elastic Parameter Sensitivity Analysis. Geofluids. https://doi.org/10.1155/2019/8750127. Article ID 8750127, 13 pages.
- Wilson, A., Chapman, M., Li, X., 2009. Frequency-dependent AVO inversion. SEG Houston 2009 International Exposition and Annual Meeting 341-345. https:// doi.org/10.1190/1.3255572.
- Wood, A.B., 1941. A Textbook of Sound. G. Bell and Sons, Ltd., London.
- Wu, X., Chapman, M., Li, X., et al., 2014. Quantitative gas saturation estimation by frequency-dependent amplitude-versus-offset analysis. Geophys. Prospect. 62, 1224-1237. https://doi.org/10.1111/1365-2478.12179.
- Yang, Z.Q., He, T., Zou, C.C., 2020. A dynamic elastic model for squirt-flow effect and its application on fluid viscosity-associated velocity dispersion in reservoir sandstones. Geophysics 85 (4), 1-48. https://doi.org/10.1190/geo2019-0312.1.
- Yenugu, M., 2014. Elastic, Microstructural and Geochemical Characterization of Kerogen Maturity for Shales. Ph.D. dissertation, University of Houston.
- Yilmaz, Ö., 2008. Seismic Data Analysis: Processing, Inversion, and Interpretation of Seismic Data. Society of Exploration Geophysicists, Tuslam, OK, USA. Page: 2021.
- Yin, X.Y., Zhang, S.X., 2014. Bayesian inversion for effective pore-fluid bulk modulus based on fluid-matrix decoupled amplitude variation with offset approximation. Geophysics 79 (5), R221-R232. https://doi.org/10.1190/GEO2013-0372.1.
- Zhang, Q.B., Guo, Z.Q., Liu, C., et al., 2018. Rock physics model and its applications in the Longmaxi shale based on the quantification of microstructural properties of organic matter. Prog. Geophys. 33 (5), 2083-2091. https://doi.org/10.6038/ pg2018BB0449 (in Chinese).
- Zhang, S., Huang, H., Dong, Y., et al., 2017. Direct estimation of the fluid properties and brittleness via elastic impedance inversion for predicting sweet spots and the fracturing area in the unconventional reservoir. J. Nat. Gas Sci. Eng. 45, 415-427. https://doi.org/10.1016/j.jngse.2017.04.028.
- Zhang, S., Yin, X., Zhang, G., 2011. Dispersion-dependent attribute and application in hydrocarbon detection. J. Geophys. Eng. 8, 498-507. https://doi.org/10.1088/ 1742-2132/8/4/002
- Zhao, L.X., Qin, X., Han, D.H., et al., 2016. Rock-physics modeling for the elastic properties of organic shale at different maturity stages. Geophysics 81 (5), 527-541. https://doi.org/10.1190/geo2015-0713.1.
- Zoeppritz, K., 1919. Erdbebenwellen VIII B, Über die reflexion und durchgang seismischer wellen durch unstetigkeitsflachen. Gottinger Nachr 1, 66–84.
- Zong, Z.Y., Yin, X.Y., Wu, G., 2013. Direct inversion for a fluid factor and its application in heterogeneous reservoirs. Geophys. Prospect. 61 (5), 998-1005. https://doi.org/10.1111/1365-2478.12038.